J. Fluid Mech. (2014), *vol.* 756, *pp.* 5–29. © Cambridge University Press 2014
doi:10.1017/jfm.2014.447

Fluid flow analysis of a shark-inspired microstructure

Samuel Martin[1] **and Bharat Bhushan**[1,†]

[1]Nanoprobe Laboratory for Bio & Nanotechnology and Biomimetics (NLBB), The Ohio State University, 201 West 19th Avenue, Columbus, OH 43210-1142, USA

(Received 6 March 2014; revised 5 June 2014; accepted 25 July 2014; first published online 1 September 2014)

The scales of fast-swimming sharks contain riblet structures with microgrooves, aligned in the direction of fluid flow, that result in water moving efficiently over the surface. In previous studies, these riblet structures have shown a drag reduction of up to 10 % when compared with a smooth, flat surface. These studies have suggested two prevalent drag-reduction mechanisms which involve the effect of vortices and turbulence fluctuations. To further explore relevant mechanisms and study the effect of riblet geometry and flow properties on drag, vortices and turbulence fluctuations, various shark-skin-inspired riblet structures were created using computational models in which velocity, viscosity, spacing, height and thickness parameters were independently modified. A relevant mechanism of drag reduction is discussed to relate riblet parameters and flow properties to drag change and vortex size. Modelling information will lead to a better understanding of riblets and allow for optimum drag-reducing designs for applications in marine, medical and industrial fields.

Key words: drag reduction, flow control

1. Introduction

Nature has produced structures and materials that are efficient and multipurpose using commonly occurring materials in order to survive. From these resourceful designs, researchers have created bioinspired designs with the goals of replicating and expanding their functionality in order to solve practical problems (Bhushan 2009, 2012). There are many aspects of nature that can serve as an inspiration for design. For example, superhydrophobicity can be found from the leaves of Lotus flowers (Bhushan 2009), reversible adhesion from the toes of a gecko (Autumn *et al.* 2000; Gao *et al.* 2005; Autumn *et al.* 2006; Bhushan 2010), antireflectivity from the eyes of moths (Genzer & Efimenko 2006) and self-cleaning from rice leaves and butterfly wings (Bixler & Bhushan 2012*b*).

A model surface inspired by nature for drag reduction is provided by shark skin. Fast-swimming sharks can quickly move through water with a low energy input. As shown in figure 1, sharks are covered in scales called dermal denticles (little skin teeth) and have riblets with microscopic grooves aligned parallel to fluid flow. The

† Email address for correspondence: bhushan.2@osu.edu

https://doi.org/10.1017/jfm.2014.447 Published online by Cambridge University Press

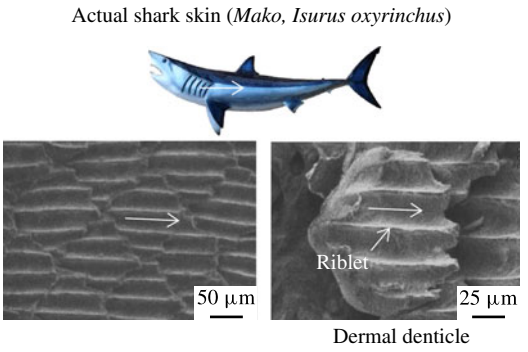


FIGURE 1. (Colour online) Scanning electron microscopy (SEM) micrographs of the skin of a fast-swimming shark from living nature shown at two magnifications (adapted from Bixler & Bhushan 2012*b*). These images highlight the scales (dermal denticles) and riblets which are responsible for drag reduction. Arrows indicate fluid flow direction.

scales are generally 0.2–0.5 mm in size with the grooves spaced 30–100 μm apart (Reif 1985; Bechert, Bruse & Hage 2000*a*,*b*; Bhushan 2012). Shark-skin-inspired riblets have been studied by various researchers both experimentally (Walsh 1982; Rohr *et al.* 1992; Bechert, Bruse & Hage 1997*b*; Lee & Lee 2001; Jung & Bhushan 2009; Dean & Bhushan 2010; Bixler & Bhushan 2012*a*, 2013) and computationally (Choi, Moin & Kim 1993; Chu & Karniadakis 1993; Goldstein, Handler & Sirovich 1995). In these studies, various riblet geometries have been examined including blade, scalloped and sawtooth designs, and riblet configurations such as continuous and segmented.

Experiments to study the drag benefits of riblets have been carried out using the so-called Berlin oil channel which contained two test plates, one with riblets and one without, inserted into a flow channel (Bechert *et al.* 1992). Force measurements on these plates were compared, and the percentage drag reduction on the riblet surface was reported using $\Delta\tau/\tau_0$ where $\Delta\tau$ is the difference in shear stress between the riblet and smooth surfaces and τ_0 is the shear stress for the smooth surface. The surface area used to calculate the shear stress was based on the smooth surface area. The riblet spacing from this experiment was non-dimensionalized using

$$s^+ = sv_\tau/\nu. \tag{1.1}$$

Non-dimensional values are denoted by a superscript $+$. In this equation, the distance between microgrooves is the riblet spacing where s is the dimensional riblet spacing, $v_\tau = (\tau_0/\rho)^{1/2}$ where v_τ is the wall shear-stress velocity, ν is the kinematic viscosity and ρ is the density. Instead of riblet spacing, García-Mayoral & Jiménez (2011) used the riblet cross-sectional area for non-dimensionalization.

Figure 2 shows the drag-reduction data for the blade, scalloped and sawtooth riblets in oil flow. The data shows a drag reduction of ∼10 % for blade, ∼6.5 % for scalloped and ∼5 % for sawtooth riblets (Bechert *et al.* 1997*b*). Although blade riblet geometries provide the greatest degree of drag reduction, due to the weak structural design of blade riblets, commercial application would be difficult; therefore, other more durable designs such as sawtooth or scalloped geometries may be desirable.

Researchers have not universally agreed upon the mechanism of drag reduction. Two main mechanisms for drag reduction that have been proposed include controlling the

https://doi.org/10.1017/jfm.2014.447 Published online by Cambridge University Press

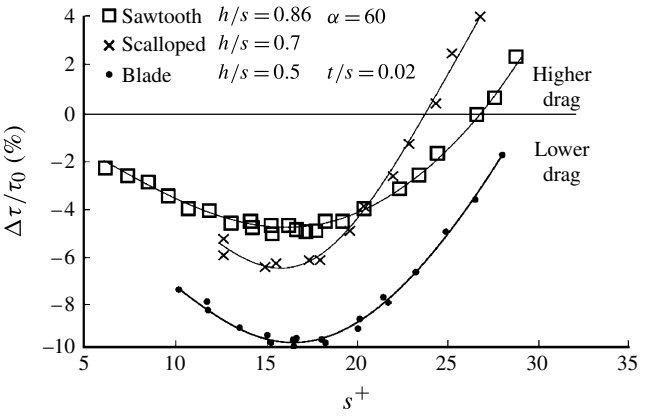


FIGURE 2. Drag-reduction curves for three continuous riblet geometries for various s^+ spacing (adapted from Bechert *et al.* 1997*b*). Blade riblets provide the greatest drag reduction followed by scalloped and sawtooth riblets. Drag reduction was calculated by measuring the force on two test plates, one with riblets and one without, and reported as $\Delta\tau/\tau_0$ where $\Delta\tau$ is the difference in shear stress between the riblet and smooth surfaces and τ_0 is the shear stress for the smooth surface. For this study, optimal spacing is at $s^+ \approx 16$ where s^+ is a non-dimensional spacing parameter defined by $s^+ = sv_\tau/\nu$ where s is the dimensional riblet spacing, $v_\tau = (\tau_0/\rho)^{1/2}$ where v_τ is the wall shear-stress velocity and ν is the kinematic viscosity. Riblet geometries are commonly non-dimensionalized in order to compare their drag change.

vortices in turbulent flow and reducing the turbulence fluctuations in the cross-flow direction (table 1).

In the first mechanism stated in table 1, riblets control the streamwise vortices that form in turbulent flow. These vortices rotate along the axis of the mean velocity direction generating ejecting and sweeping motions in which high-velocity fluid mixes with the low-velocity fluid near the surface. Consequently, this motion creates zones of high shear stress and drag. By choosing an appropriately sized riblet spacing based on the vortex size inherent to the flow, these vortices can be lifted away from the surface, decreasing the area exposed to high shear stress and therefore reduce drag (Kim, Moin & Moser 1987; Choi *et al.* 1993; Lee & Lee 2001).

In the second mechanism stated in table 1, riblets decrease the fluctuating velocity component in the cross-flow direction. In turbulent flow, the flow is unsteady, and the fluid velocity oscillates around the mean flow velocity. By channelling the flow using riblets, this oscillation is reduced; therefore, the momentum transfer close to the surface and overall drag is reduced. An effective protrusion height parameter has been suggested to measure the riblet geometry effectiveness in reducing drag. This parameter is the difference between the streamwise and cross-flow protrusion heights shown in table 1 (Bechert *et al.* 1986; Bechert & Bartenwerfer 1989). The effective protrusion height parameter (Δh) increases with increased spacing (s) because Δh is a constant fraction of the riblet spacing. With a larger spacing, the turbulent cross-flow and momentum exchange near the wall decreases and therefore the cross-flow protrusion height decreases. With riblets with small spacing only interacting in the viscous regime, a linear relationship is expected due to the law of the wall, which is the relationship between the velocity at the wall and the distance from the wall in non-dimensional units (Spalding 1961) and so the initial slope of the drag reduction curve is proportional to $(\Delta h/s)s^+$ (Bechert *et al.* 1997*b*).

https://doi.org/10.1017/jfm.2014.447 Published online by Cambridge University Press

https://doi.org/10.1017/jfm.2014.447 Published online by Cambridge University Press

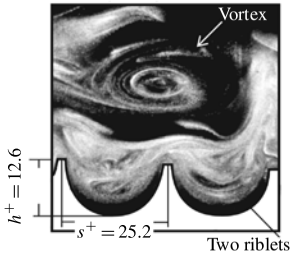
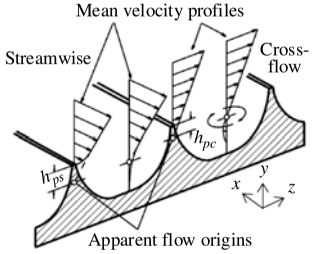
Image	Observations	Questions
 Flow visualization of a vortex interacting with a riblet surface using smoke in air from atomized oil (adapted from Lee & Lee, 2001).	Riblets with appropriately sized spacing reduce viscous drag by lifting and pinning the streamwise vortices away from the surface and decreasing the mixing of high- and low-speed fluid. However, with a small spacing, vortices contact many riblet peaks leading to many high-shear-stress zones; with a large spacing, vortices can fall into the riblet valleys, exposing the surface to high-speed fluid (Choi *et al.* 1993). Previous computational work has suggested average vortex diameters of ~30 wall units (s^+) and located at ~20 wall units from the surface (Kim *et al.* 1987) and experimental work has shown average vortex diameters of 30–40 wall units (Lee & Lee 2001).	Previous studies varied velocity or non-dimensionalized the riblet parameters, which does not fully explain the effect of individually varying riblet parameters such as spacing (s^+; peak-to-peak distance), height (h^+; peak-to-valley distance), or thickness (t^+; peak width) on drag and vortex size.
 Schematic of the mean velocity profiles for flow in the streamwise and cross-flow dirctions (adapted from Bechert *et al.*, 1997*b*)	Riblets channel the flow in the mean x-direction by reducing the fluctuating turbulent cross-flow velocity component in the z-direction. This obstruction reduces the turbulent momentum transfer close to the surface leading to a drag reduction. The effective protrusion height parameter (Δh) is a measure of how effectively the riblets reduce drag and is the difference between the streamwise (h_{ps}) and cross-flow protrusion heights (h_{ps}) (Bechert *et al.* 1986; Bechert & Bartenwerfer 1989). At low s^+, the drag reduction was found to be proportional to $(\Delta h/s)s^+$ (Bechert *et al.* 1997*b*).	Previous computational work (Choi *et al.* 1993; Goldstein *et al.* 1995) and experimental work (Weiss 1993; Suzuki & Kasagi 1994) have shown decreased cross-flow fluctuations; however, various riblet parameters have not been modified to see the change in turbulent cross-flow velocity component and compared with the overall drag change.

TABLE 1. Two ideas for the riblet drag-reduction mechanism. The first idea shows an image of a lifted vortex created by atomizing oil burned in air to produce smoke. With appropriate sized riblet spacing, vortices are lifted away from the surface decreasing the ejecting and sweeping motions. The second idea shows an image of the effective protrusion height parameter which is a calculation to show the efficiency of the riblet geometry in channelling the fluid and reducing the cross-flow turbulence fluctuations.

Researchers do not fully understand the mechanism of drag reduction and have primarily suggested these mechanisms as possible explanations. Furthermore, from the definition of s^+, the drag reduction should be the same for constant non-dimensional parameters even if the spacing, velocity or viscosity terms are changed. This concept has not been explored, and limited drag data can be compared to answer whether this definition holds. In addition, it is not understood how the effect of riblet geometry and flow properties impacts on drag, vortex size and turbulence fluctuations. The size of vortices has been measured for limited geometries and Reynolds numbers, and turbulence fluctuations have not been compared with drag change for various riblet geometry.

By investigating and answering these concerns, riblets can become more widely implemented in commercial applications as a method of drag reduction. For example, riblet technology has applications in competitive swimsuits; air, water and oil pipe flow; and transportation. Currently, riblet technology has been employed in competitive swimwear such as the Speedo Fastskin® swimsuit to reportedly decrease drag by up to 4 % (Krieger 2004). Applying riblets to the inside of pipes would decrease drag (Bechert, Bruse & Hage 1997*a*; Weiss 1997) and reduce fouling in oil and water flow (Bixler & Bhushan 2012*a*,*b*). In oil pipeline flow, sludge accumulation causes high drag and requires higher pumping energy. In ships, biofouling in which aquatic growth accumulates on the hull also increases drag. Riblets could be applied to the hull of ships to reduce fouling and create a drag reduction. To investigate reducing skin friction drag on aircraft using riblet structures, studies at the National Aeronautics and Space Administration's Langley Research Center (Walsh & Anders 1989) and the German Aerospace Center (Bechert *et al.* 1997*a*) have been carried out. Riblets by covering approximately 70 % of the hull of an aircraft can provide a 3 % drag reduction resulting in desirable fuel savings (Bechert *et al.* 1997*a*).

In this paper, a computational fluid dynamic (CFD) model of blade riblet structures was created in order to study drag, vortex formations and turbulence fluctuations. These insights will help determine which of the two proposed riblet mechanisms is relevant and help to develop optimal riblet designs. In addition, the definition of riblet spacing can be evaluated to determine whether it is a valid non-dimensional parameter in determining drag. To answer these questions, two fluid parameters (velocity and viscosity) and three riblet parameters (spacing, height and thickness) for blade riblets were independently changed.

2. Modelling

In this section, the CFD program and turbulence model will be presented first. Next, a validation model of the flow around a square cylinder will be shown. Lastly, the shark-skin inspired riblet models are presented along with the methods to analyse the flow results.

2.1. *CFD program*

ANSYS® FLUENT 14.0 was used as the CFD software, and the large eddy simulation (LES) model with the Smagorinsky–Lilly subgrid scale was used to analyse the flow. LES resolves the large-scale flow eddies and models the small-scale flow eddies which results in greater accuracy over a Reynolds-averaged Navier–Stokes (RANS) model.

https://doi.org/10.1017/jfm.2014.447 Published online by Cambridge University Press

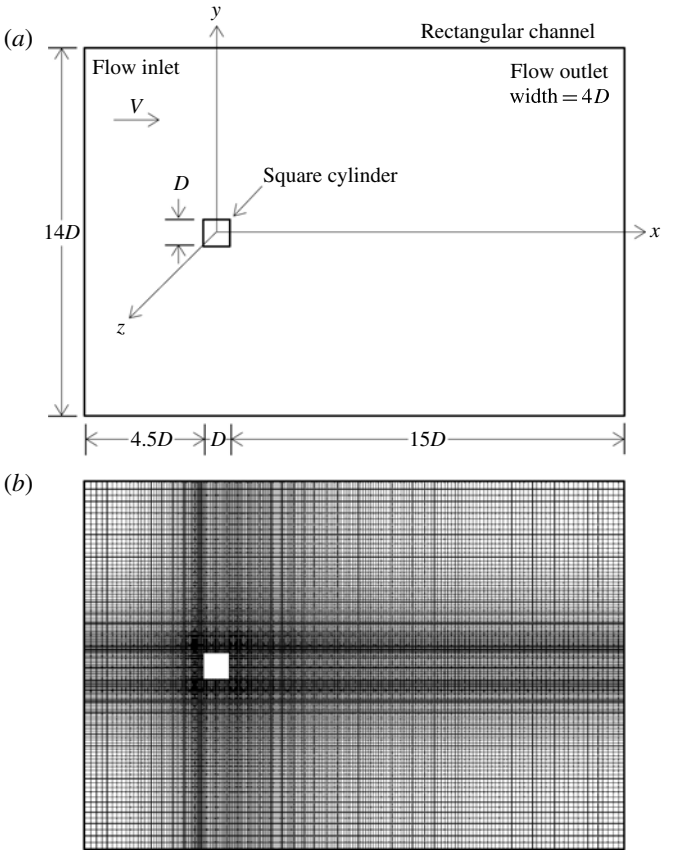


FIGURE 3. Side view of the flow in a rectangular channel with a square cylinder for LES validation showing geometry (*a*) and mesh (*b*). Computational mesh of the geometry is $220 \times 150 \times 20$.

2.2. *Validation model: flow around a square cylinder*

In order to validate the performance of this model, turbulent flow over a square cylinder with edge length $D = 0.04$ m was performed. This simulation is a well-documented experimental (Vickery 1966; Lee 1975; Cheng, Lu & Chen 1992; McLean & Gartshore 1992; Lyn & Rodi 1994; Lyn *et al.* 1995) and computational test case for the LES model (Murakami & Mochida 1995; Rodi 1997; Rodi *et al.* 1997; Ochoa & Fueyo 2004). The dimensions of the domain were normalized by this edge length as shown in figure 3. The x, y and z axes denote the streamwise, wall-normal and spanwise or cross-flow directions, respectively, and V denotes the average velocity in the streamwise direction.

The inlet boundary condition was specified as a uniform velocity of 0.535 m s^{-1} with no added perturbations which corresponded to a Reynolds number of 21 400 in order to compare with the published data. The top and bottom surfaces were prescribed as no-slip wall boundary conditions and the left and right surfaces were prescribed as periodic boundary conditions. The computational mesh was $220 \times 150 \times 20$ along the x, y, and z directions, respectively. The mesh was refined in the region near the square cylinder as well as behind the cylinder to resolve the flow more accurately.

https://doi.org/10.1017/jfm.2014.447 Published online by Cambridge University Press

Reference	$\bar{C}_L$	C_L^{rms}	$\bar{C}_D$	C_D^{rms}	St
Numerical data – from Ochoa & Fueyo (2004)					
Verstappen and Veldman	0.005	1.45	2.09	0.178	0.133
Porquie *et al.*					
—	−0.02	1.01	2.2	0.14	0.13
—	−0.04	1.12	2.3	0.14	0.13
—	−0.05	1.02	2.23	0.13	0.13
Murakami & Mochida (1995)	−0.05	1.39	2.05	0.12	0.131
Wang and Vanka	0.04	1.29	2.03	0.18	0.13
Nozawa and Tamura	0.0093	1.39	2.62	0.23	0.131
Kawashima and Kawamura					
—	0.01	1.26	2.72	0.28	0.16
—	0.009	1.38	2.78	0.28	0.161
Ochoa & Fueyo (2004)	0.03	1.4	2.01	0.22	0.139
Experimental data					
Vickery (1966)	—	0.68–1.32	2.05	—	—
Lee (1975)	—	—	2.05	0.16–0.23	—
Cheng *et al.* (1992)	—	0.1–0.6	1.9–2.1	0.1–0.2	—
McLean & Gartshore (1992)	—	0.7–1.4	1.9–2.1	0.1–0.2	—
Lyn & Rodi (1994), Lyn *et al.* (1995)	—	—	2.1	—	0.132
This work ($D = 0.04$ m, $V = 0.535$ m s^{-1}, $Re = 21\,400$)	−0.04	1.41	2.28	0.16	0.130

TABLE 2. Comparison among time-averaged square cylinder data.

A time step of 2.5×10^{-3} s was used for 10 000 time steps. This time step was chosen to resolve the flow using the Courant condition which allows for the calculations to capture the time scales at the cell residence time. The data was averaged over the last 7000 time steps which was approximately 11 times the residence time. From published experimental and numerical results, the mean lift coefficient, $\bar{C}_L$, lift oscillation amplitude, C_L^{rms}, mean drag coefficient, $\bar{C}_D$, drag oscillation amplitude, C_D^{rms}, and Strouhal number, St, were compared with the results of the test case. It can be seen in table 2 that the results for this work agree and so this model was validated for use in modelling riblet structures.

2.3. *Shark-skin inspired riblet models*

The cases that were analysed are presented in table 3. The variables that were independently changed included two fluid parameters (velocity V and viscosity ν) and three riblet parameters (spacing s, height h and thickness t). In the table, the dimensional values are presented on the left, and the resulting non-dimensional values are presented on the right. The values were non-dimensionalized using the wall shear-stress velocity. The non-dimensional riblet spacing parameter has been given in (1.1). Similarly, the height (h) and thickness (t) were non-dimensionalized as $h^+ = hv_\tau/\nu$ and $t^+ = tv_\tau/\nu$, respectively.

In order to run a computer model, the dimensional parameters V, ν, s, h and t needed to be chosen. Because the Reynolds number and non-dimensional riblet parameters s^+, h^+ and t^+ are the variables controlling the flow phenomenon, linearity between V and v_τ must be shown to satisfy (1.1). Using the wall shear-stress velocity

https://doi.org/10.1017/jfm.2014.447 Published online by Cambridge University Press

https://doi.org/10.1017/jfm.2014.447 Published online by Cambridge University Press

	s (mm)	h (mm)	t (μm)	ν/V_l (μm)		s^+	h^+	t^+	Number of riblets
				Varying V_l $\nu = 10^{-6}$ m^2 s^{-1}	Varying ν $V_l = 0.42$ m s^{-1}				
Baseline	**1.00**	**0.50**	**20.0**	**2.38**	**2.38**	**16.2**	**8.1**	**0.32**	**20**
Effect of V				4.00		10.3	5.1	0.21	20
				2.38		**16.2**	**8.1**	**0.32**	**20**
				1.39		24.5	12.3	0.49	20
				0.98		32.4	16.2	0.65	20
				0.76		46.8	23.4	0.94	20
Effect of ν					4.00	10.7	5.4	0.21	20
					2.38	**16.2**	**8.1**	**0.32**	**20**
					1.39	27.4	13.7	0.55	20
					0.77	46.7	23.3	0.93	20
Effect of s	0.50					8.4	8.4	0.34	40
	1.00					**16.2**	**8.1**	**0.32**	**20**
	1.50					25.3	8.4	0.34	13
	2.50					41.1	8.2	0.33	8
Effect of h		0.25				16.2	4.1	0.32	20
		0.50				**16.2**	**8.1**	**0.32**	**20**
		0.75				16.6	12.5	0.33	20
	0.75	0.22	15.0	1.20		22.9	6.7	0.46	27
	0.75	0.32	15.0	1.20		23.2	9.9	0.46	27
	0.75	0.42	15.0	1.20		23.2	13.0	0.46	27
Effect of t			5.0			16.8	8.4	0.08	20
			10.0			17.0	8.5	0.17	20
			20.0			**16.2**	**8.1**	**0.32**	**20**
			30.0			16.6	8.3	0.50	20

TABLE 3. Test cases for the simulations of turbulent flow over riblets.

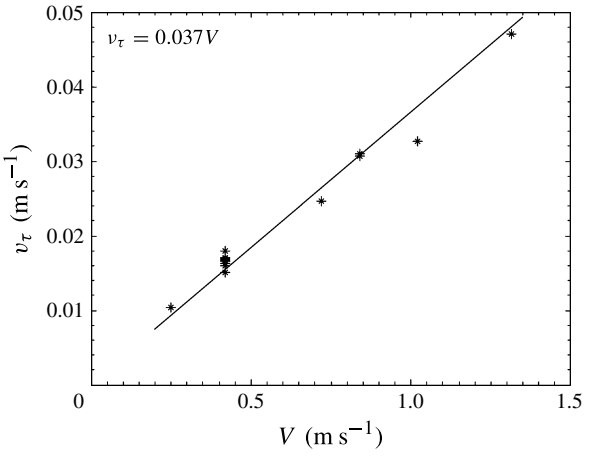


FIGURE 4. Wall shear-stress velocity compared with velocity showing a linear relationship which allows for changing velocity as a means to modify the wall shear-stress velocity.

and velocity from the test cases in table 3, figure 4 shows wall shear-stress velocity compared with velocity. Because the relationship was approximately linear, changing the velocity will linearly change the wall shear-stress velocity, and (1.1) could be used to non-dimensionalize the riblet parameters. Therefore, the data trends presented in this paper are independent of the dimensions selected for the models.

For the test cases with varying velocity or viscosity, either the viscosity or the velocity was held constant and was listed in the table as ν/V_l. For the effect of velocity cases, the viscosity was held constant at $\nu = 10^{-6}$ m^2 s^{-1}; for the effect of viscosity cases, the velocity was held constant at $V_l = 0.42$ m s^{-1}. The baseline values shown in bold numbers in the table were chosen for blank cells.

The values of the dimensional parameters were chosen to fulfil several requirements. First, they were chosen over a range, such that when they were non-dimensionalized, the cases would cover a wide non-dimensionalized range for the parameter. Second, the values were selected so that the non-dimensional values could be compared with the other cases. By having similar non-dimensional values that were created by modifying different dimensional parameters, the definition of non-dimensionalizing could be explored. Lastly, the dimensional values were chosen so that s^+ of 15–20 would be in the centre of the parameter's ranges. In other studies, this range has been shown for optimal drag reduction. By centring the data on this value, it would allow for test cases on either side of this range to be investigated.

Two sets of riblet height test cases were created to further explore the relationship between riblet height and drag. In the first set, only the height was modified so the other parameters were kept the same as the baseline case. In the second set, all of the parameters were modified to increase the Reynolds number, centre s^+ near 23 and h^+ near 10.

2.3.1. *Model set-up*

Figure 5 shows that the models were created with the riblet surface on the bottom wall and the smooth surface on the top wall. These walls had the no-slip boundary condition. With both surfaces in the model, the drag change for the riblet surface

https://doi.org/10.1017/jfm.2014.447 Published online by Cambridge University Press

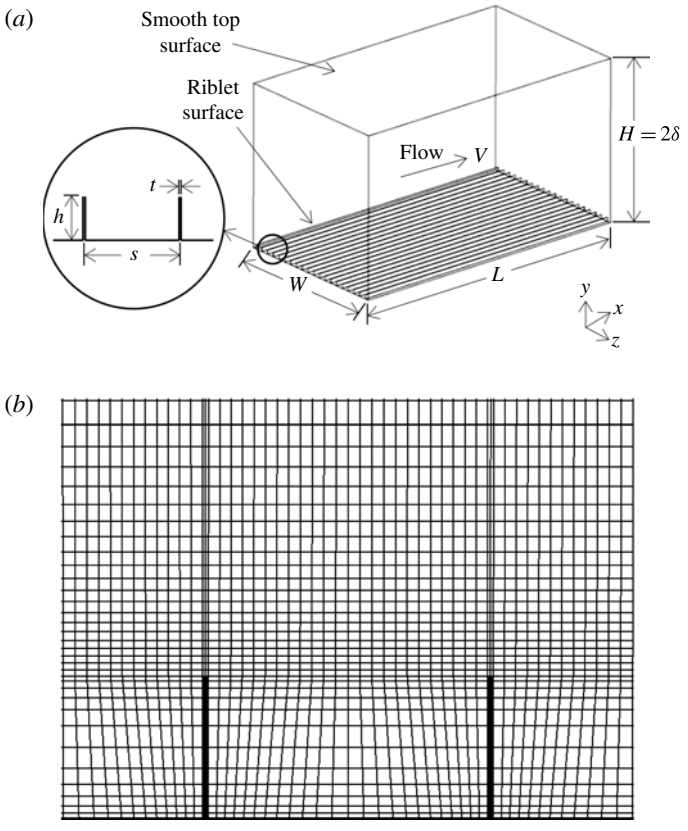


FIGURE 5. (*a*) Computational domain of the riblet geometry for the baseline case showing geometry and the riblet dimensions. Twenty riblets are on the bottom surface and a smooth surface is on the top surface for drag comparison. (*b*) Computational mesh near riblets.

can be directly compared with the smooth surface. The x, y, and z axes denote the streamwise, wall-normal and spanwise or cross-flow directions, respectively.

Along the streamwise direction, a constant instantaneous volume flux boundary condition was applied,

$$Q = \int_{A_c} V \, \mathrm{d}A_c = \frac{2}{3} A_c V_l \tag{2.1}$$

where $A_c = HW$ is the cross-sectional area, V is the average velocity in the streamwise direction and V_l is the centreline velocity of a laminar parabolic profile with the same volume flux. The Reynolds number was calculated with δ as the channel half-width ($\delta = H/2$) using

$$Re = V_l \delta / \nu. \tag{2.2}$$

The inlet and outlet surfaces and the left and right surfaces were prescribed as periodic so that wall effects would not interfere with the results. The solution was initialized with a laminar velocity profile and afterwards turbulence fluctuations were added. The solution was advanced using a computational time step of $\Delta T V_l/\delta = 0.05$ where ΔT is the dimensional time step until natural turbulence was developed by monitoring wall-shear stresses for quasi-periodic behaviour. After a statistically steady

https://doi.org/10.1017/jfm.2014.447 Published online by Cambridge University Press

flow field was reached, the simulations were continued for additional time to time average the results.

The computational domain dimensions were chosen to be large enough to include the expected scales of the flow structures and to be greater than the minimal flow unit (100 wall units in the spanwise direction and 300 wall units in the streamwise direction where a wall unit is non-dimensionalized as in (1.1) using a length scale such as the spanwise or streamwise distance, respectively) as determined by Jimenez & Moin (1991). For the models, the height H and width W remained constant at 0.02 m which corresponded to 206 wall units in the smallest case. The length L changed for the cases to keep a grid spacing at $x^+ \approx 35$ and with 16 nodes this corresponds to approximately 560 wall units in length. In the spanwise direction, the z^+ grid spacing varied between 0.4 and 2.0 with the resolution $z^+ \approx 0.7$ for most cases. In the wall-normal direction, there were 128 grid points with the first grid point on the smooth surface baseline case at $y^+ = 0.16$. Furthermore, it was kept below $y^+ = 1$ for all cases as required by the LES model, and the mesh was biased towards the surfaces to capture the flow field near the walls more accurately. The grid resolution was kept the same on the smooth and riblet surfaces for drag comparison purposes.

In a study by Choi *et al.* (1993), the number of grid points in the streamwise and spanwise direction was increased from $16 \times 129 \times 32$ to $32 \times 129 \times 64$ to investigate the influence of grid resolution on turbulence statistics. Doubling the grid points in the streamwise and spanwise directions changed the maximum turbulence intensities and Reynolds shear stresses by less than 2 %. The grid resolution in the streamwise and spanwise direction was approximately the same as Choi *et al.* (1993) and finer than Kim *et al.* (1987). Also, the grid resolution was much finer than the recommended requirements of $x^+ = 40$ and $z^+ = 20$ suggested by FLUENT (2014).

To determine the error bounds using the grid resolution and time averaging length for these models, the drag on two smooth walls in a plane channel flow were compared by time averaging over 500 non-dimensional time steps (T^+) where $T^+ = T\ V_l/\delta$. A solution with enough time averaging should yield identical drag on the surfaces. After averaging the drag over $T^+ = 500$, the drag on the plane walls differed by ± 2 % of each other. This percentage was in agreement with the drag variations in Walsh (1982) and Choi *et al.* (1993).

2.3.2. *Drag, vortex and turbulence fluctuation measurement*

The instantaneous skin-friction drag for the smooth surface, D_s, and riblet surface, D_r, were calculated with

$$\left.\begin{aligned} D_s &= \mu \int_{A_s} \frac{\partial u}{\partial n} \mathrm{d}A_s \\ D_r &= \mu \int_{A_r} \frac{\partial u}{\partial n} \mathrm{d}A_r \end{aligned}\right\} \tag{2.3}$$

where n is the coordinate normal to the surface, and A_s and A_r are the surface areas for the smooth and riblet surfaces, respectively. Figure 6 shows that the instantaneous drag for the riblet and smooth surfaces was quasi-periodic. To calculate the time-averaged drag, the drag on each surface was averaged over a time period of at least $T^+ = 500$. The percentage drag change was calculated by comparing the time-averaged drag for these two surfaces as $(\bar{D}_r - \bar{D}_s)/\bar{D}_s$.

At time intervals of $T^+ = 50$, four equally spaced y–z planes with vorticity contours and tangential velocity vectors were plotted. These images were used to measure the

https://doi.org/10.1017/jfm.2014.447 Published online by Cambridge University Press

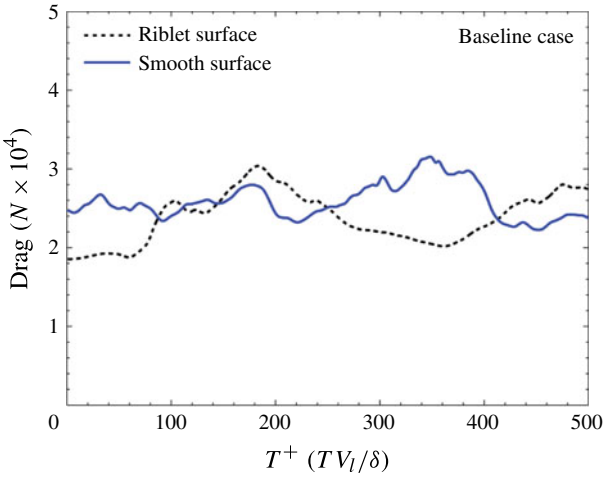


FIGURE 6. (Colour online) Time history of drag on the riblet and smooth surfaces. Due to turbulence, the drag on each surface changes with time. The simulation was run for at least 500 non-dimensionalized time units (T^+) to average the drag on each surface. This figure shows an 8 % drag reduction on the riblet surface.

height, width and vortex centre distance from the wall for vortices in the buffer layer (5–30 non-dimensionalized wall units from the wall) on the riblet and smooth surfaces, as illustrated in figure 7. For each case over a time of $T^+ = 500$, this resulted in 44 images to analyse. The vortex size data taken from these images was averaged for each case and will be presented to explain a possible riblet mechanism.

The definition of a vortex by Robinson (1990) states that 'A vortex exists when instantaneous streamlines mapped onto a plane normal to the vortex core exhibit a roughly circular or spiral pattern, when viewed from a reference frame moving with the center of the vortex core'. This definition was used to measure the quasi-streamwise vortices located in the buffer layer (Robinson 1990) with the vortex boundary defined as the edges at which the spinning motion of the fluid shown by the velocity vectors began to break down. Vorticity plots were not used by themselves to determine vortices because strong vorticity is not entirely indicative of actual vortices especially near the walls (Robinson, Kline & Spalart 1989). For example, at the riblet peaks in figure 7, strong vorticity was seen, but the velocity vectors do not suggest a vortex at the peaks.

To measure the turbulence fluctuation in the cross-flow direction, points in the model were created. These points were located at the centre of the riblet valleys (half the riblet height and half the riblet spacing) and at the corresponding locations on the smooth surface. The root-mean-square (r.m.s.) of the cross-flow turbulence fluctuation was recorded at these points. The reduction in cross-flow turbulence was defined as $(w'_s - w'_r)/w'_s$, where w'_s and w'_r are the r.m.s. cross-flow turbulence fluctuations for the smooth and riblet surfaces, respectively. This data was used to view the relationship between riblet geometry and the reduction in turbulence fluctuations as explained in the second riblet mechanism.

3. Results and discussion

In this section, the drag, vortex size and turbulence fluctuations data will be presented to evaluate the performance of these riblets. This data was used to compare

https://doi.org/10.1017/jfm.2014.447 Published online by Cambridge University Press

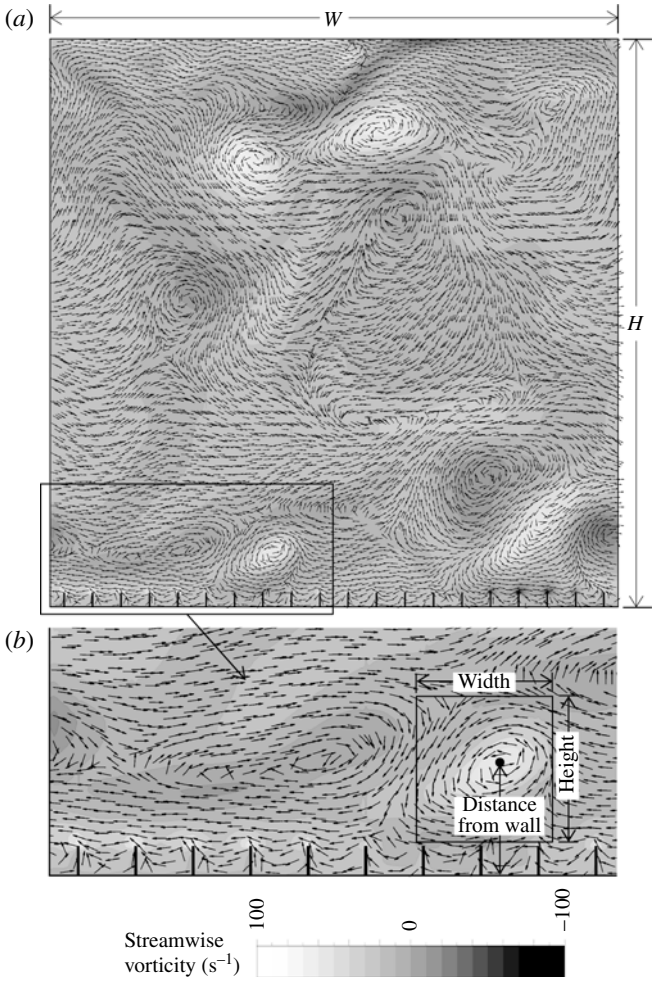


FIGURE 7. Contour plot of streamwise vorticity and tangential velocity vectors on an y–z plane showing the effects of turbulence. The height, width and distance from a wall for an example vortex are presented. The parameters used in the image are $s = 1.00$ mm, $h = 0.50$ mm, $t = 20.0$ μm, $\nu/V_l = 2.38$ μm and $Re = 4180$.

the two possible mechanisms of drag reduction and present how riblet parameters affect drag change and vortex size.

3.1. *Drag change*

In figure 8, the drag change for the various models was plotted with negative values denoting a drag-reduction benefit. In figure 8(*a*) with varying velocity and viscosity, both curves have similar trends with a maximum drag reduction at $s^+ = 18$–20 of 9 % and 12 %. Independently, the velocity and viscosity terms yielded approximately the same drag reductions. Because of this similarity, the non-dimensional equation was validated. The non-dimensional parameters will give the same drag change regardless of which parameters in the non-dimensional definition are modified.

https://doi.org/10.1017/jfm.2014.447 Published online by Cambridge University Press

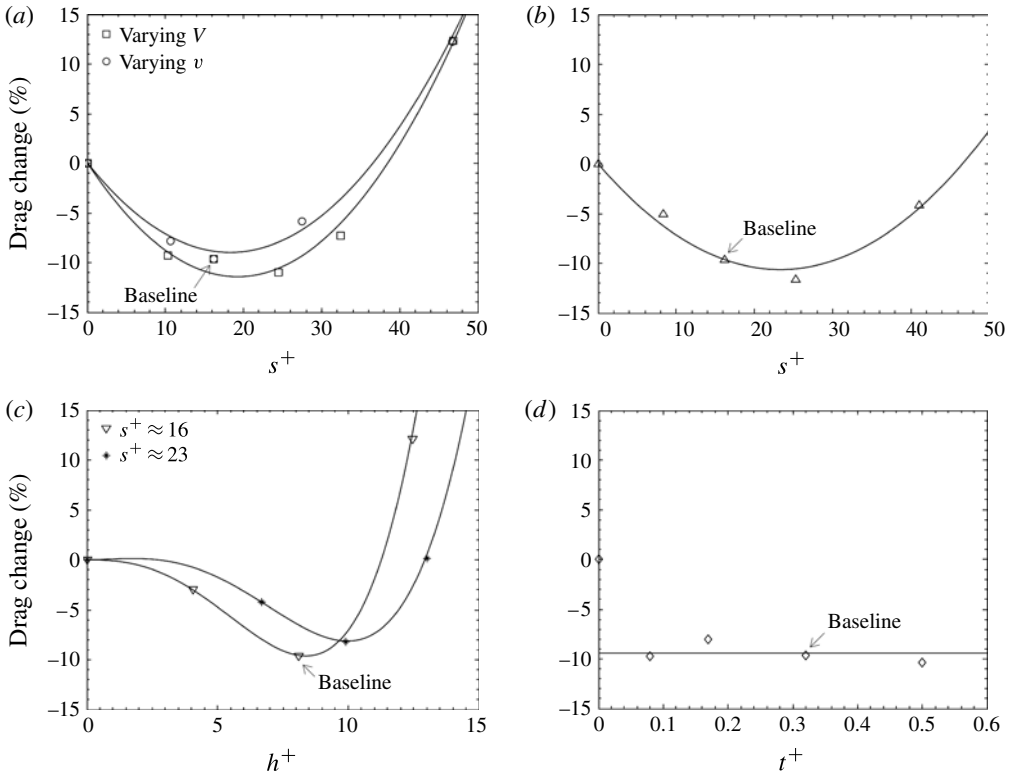


FIGURE 8. Drag change for the various models plotted against their non-dimensionalized parameter. The data used in the analyses is for: (*a*) varying V or ν $s = 1.00$ mm, $h = 0.50$ mm, $t = 20.0$ μm, $Re = 2500$–$13\,000$; (*b*) varying s $h = 0.50$ mm, $t = 20.0$ μm, $\nu/V_l = 2.38$ μm, $Re = 4180$; (*c*) varying h downward-pointing triangle $s = 1.00$ mm, $t = 20.0$ μm, $\nu/V_l = 2.38$ μm, $Re = 4180$; asterisk $s = 0.75$ mm, $t = 15.0$ μm, $\nu/V_l = 1.20$ μm, $Re = 8360$; (*d*) varying t $s = 1.00$ mm, $h = 0.50$ mm, $\nu/V_l = 2.38$ μm, $Re = 4180$. In the models with varying velocity, viscosity or spacing (*a*,*b*), the curves agree to a first order. At higher s values and constant h values, the h/s ratio becomes small leading to a slightly different curve (*b*). From the models with varying velocity or viscosity (*a*), optimal spacing was found to be at $s^+ \approx 18$–20. From the models with varying spacing (*b*), optimal spacing was found to be at $s^+ \approx 23$. From the models with varying height (*c*), optimal height was found to be at $h^+ \approx 8$–10. The s^+ and h^+ terms affect drag significantly, whereas this range of t^+ did not affect drag notably as shown in (*d*).

In figure 8(*b*) with varying spacing, the drag reduction minimum of 11 % was located at $s^+ = 23$. Even though the spacing was modified similarly to the models with varying velocity or viscosity, the spacing curve did not match the velocity or viscosity curve. This discrepancy was due to the riblet height and thickness not being affected by modifying the spacing term. Changing velocity or viscosity resulted in changing non-dimensional spacing, height and thickness; however, changing spacing only resulted in changing non-dimensional spacing. In the models with varying spacing, the height remained constant, and a greater non-dimensional riblet spacing was required for the riblets to reach a drag increasing state. Due to the differences between the velocity and viscosity curves and the spacing curve, it was apparent that both riblet spacing and height played a large role in determining drag change.

https://doi.org/10.1017/jfm.2014.447 Published online by Cambridge University Press

Furthermore, in figure 8(*c*) with varying height and constant spacing, there was a dramatic drag change between the baseline case and the taller riblet case for $s^+ \approx 16$. In the baseline case, there was a drag reduction of nearly 10 % with $h^+ = 8.1$, but in the taller riblet case, there was a drag increase of 12 % with $h^+ = 12.5$. Similarly with $s^+ \approx 23$, there was a drag reduction of 8.2 % at $h^+ = 9.9$ with less of a drag reduction on either side of this case. A height in the region of $h^+ = 8$–10 optimally reduced drag for both cases even with different Reynolds numbers and riblet spacings; however, increasing outside of this range quickly led to a drag increasing state and decreasing outside this range led to less efficient state.

When the riblet thickness was modified, little drag change occurred (figure 8*d*). The thicknesses ranged from $t^+ = 0.08$–0.50, and the drag reduction was found to be roughly constant at approximately 9 %. There were slight oscillations around this value, but because there was not a strong positive or negative relationship, the trend was reported as constant over this range of thicknesses. At much larger thicknesses, the riblet valley width would decrease and the surface area at the riblet peaks would increase. It is expected that these changes would generate a weaker drag reduction, and eventually a drag increase.

3.2. *Vortex height and width*

Using the y–z planes with vorticity contours and tangential velocity vectors, the height and width of the streamwise vortices were measured and averaged. In figure 9, the average vortex height and width on the smooth and riblet surface were plotted. As the velocity was increased in figure 9(*a*), the height and width of the vortices became larger on both surfaces. In figure 9(*b–d*) for varying spacing, height and thickness, the vortex size was fairly constant. In these figures, the smooth surface vortex width averaged 37 wall units; the riblet surface vortex width averaged 32 wall units; the smooth surface vortex height averaged 23 wall units; and the riblet surface vortex height averaged 19 wall units.

The size of the vortices was related to the Reynolds number based on the channel height. In the models with varying velocity or viscosity, the Reynolds number was changing, and so the vortex height and width changed. Because the varying spacing, height and thickness cases had the same Reynolds number of 4180, the vortex size data was approximately the same for each of these cases.

On both surfaces, the vortex width was larger than the vortex height. For the vortex height and width, the smooth surface had larger sizes than the riblet surface. Because the sides of the model used periodic conditions, the vortices could grow in the width direction; however, the riblet and smooth surfaces impeded the growth in the height direction. The vortex sizes on the riblet surface were smaller than the smooth surface because the riblets protruded sharply into the flow obstructing vortex rotation and growth.

The vortex sizes from this research are in good agreement with the vortex sizes suggested by Kim *et al.* (1987) and Lee & Lee (2001) for comparable Reynolds numbers. In Kim *et al.* (1987), it was suggested that the streamwise vortices were 30 wall units in diameter at a Reynolds number of 3300. The work by Lee and Lee was done at Reynolds numbers 2340 and 4950 and showed vortex diameters of 30–40 wall units.

The drag change and vortex size data were compared to determine when the drag had a lowest value. The optimal drag reduction was located at $s^+ = 18$–20 and $s^+ = 23$ from figure 8(*a,b*), respectively. By comparing these s^+ values with the riblet surface

https://doi.org/10.1017/jfm.2014.447 Published online by Cambridge University Press

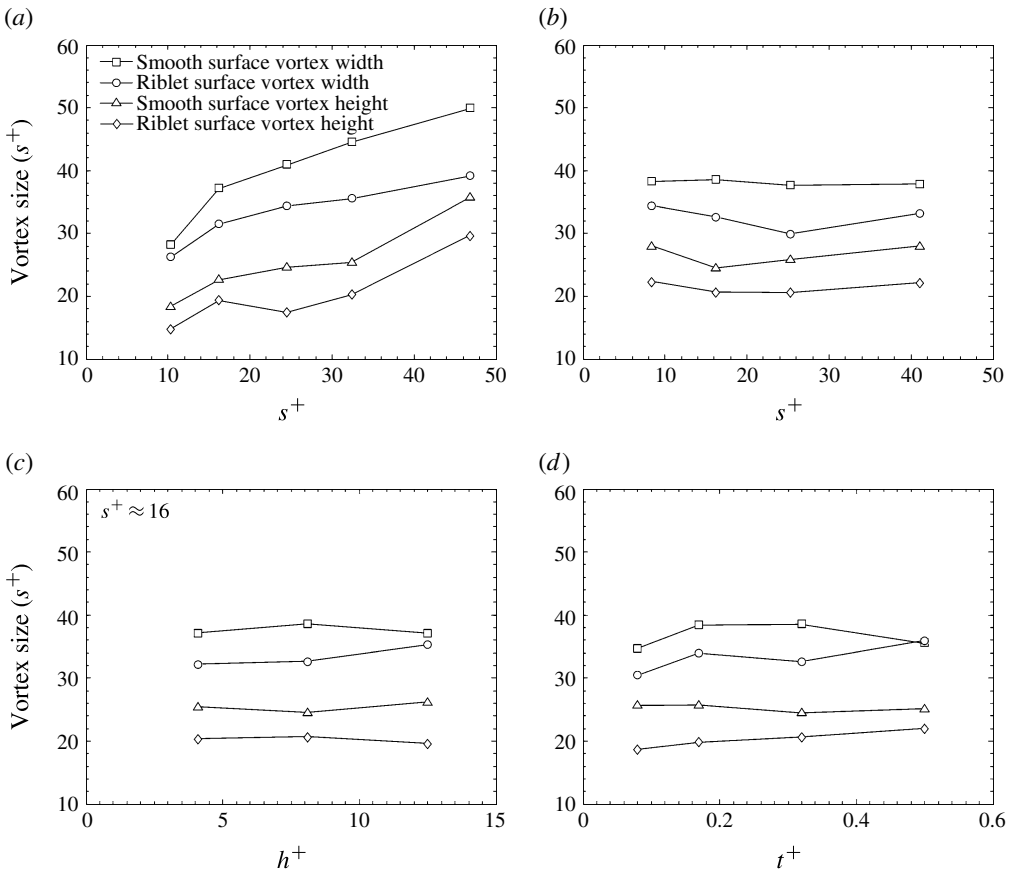


FIGURE 9. Vortex height and width on the riblet and smooth surfaces for the various models. The data used in the analyses is for: (*a*) varying V $s = 1.00$ mm, $h = 0.50$ mm, $t = 20.0$ μm, $Re = 2500$–$13\,000$; (*b*) varying s $h = 0.50$ mm, $t = 20.0$ μm, $\nu/V_l = 2.38$ μm, $Re = 4180$; (*c*) varying h $s = 1.00$ mm, $t = 20.0$ μm, $\nu/V_l = 2.38$ μm, $Re = 4180$; (*d*) varying t $s = 1.00$ mm, $h = 0.50$ mm, $\nu/V_l = 2.38$ μm, $Re = 4180$. With increasing velocity (*a*), Reynolds number based on channel height and vortex size increases. In the models with varying s, h or t (*b*)–(*d*), vortex size remains approximately constant. Average vortices have a greater width than height, and vortices on the smooth surface are larger than on the riblet surface. Riblets pin the vortex keeping them from growing and becoming the same size as the vortices on the smooth surface.

vortex width on figure 9(*a,b*), it was found that the average riblet surface vortex width was approximately 32 non-dimensional units. This corresponded to a vortex-width-to-spacing ratio of approximately 1.5. As the spacing and riblet surface vortex width approached the same value, the drag became larger and eventually became a drag-increasing case. It is thought that this ratio is effective in lifting away the vortices from the surface and minimizing the exchange of high-velocity and low-velocity fluid. As the size of the vortices and spacing approached the same value, there was a greater possibility of a vortex fitting within a riblet valley and increasing drag.

The average vortex centre distance from the wall was plotted for the models with varying spacing in figure 10. As s^+ increased, the vortices were lifted less on the riblet

https://doi.org/10.1017/jfm.2014.447 Published online by Cambridge University Press

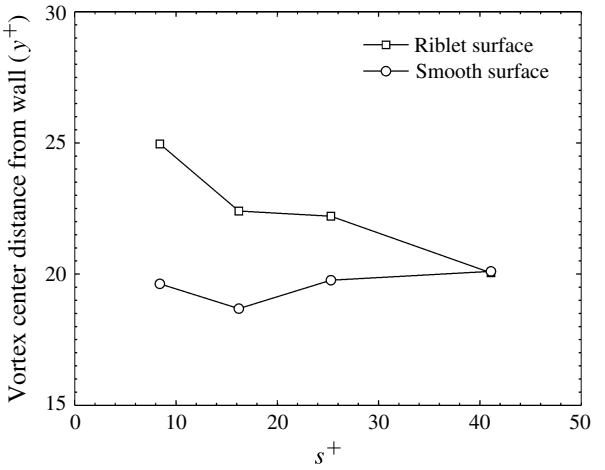


FIGURE 10. Vortex centre distance from the wall on the riblet and smooth surfaces for the models with varying spacing. The data used in the analyses is for $h = 0.50$ mm, $t = 20.0$ μm, $\nu/V_l = 2.38$ μm and $Re = 4180$. As s^+ increases, vortex centre distance from the wall decreases on the riblet surface and stays approximately constant on the smooth surface.

surface and stayed at $y^+ \approx 20$ on the smooth surface. At small spacing, riblets lift up the vortices, but have a much larger surface area. At large spacing, riblets do not lift up the vortices. When the spacing was $s^+ \approx 20$, vortices were lifted from the riblet wall without dramatically increasing the surface area and a greater drag reduction was observed.

3.3. *Turbulence fluctuations*

The reduction in cross-flow turbulence fluctuations was plotted in figure 11. In the models with varying s^+ (figure 11*a,b*), the largest reduction was at small non-dimensional spacing. As the spacing increased, more cross-flow turbulence was observed in the riblet valleys. At larger spacings, the fluid was further from the no-slip condition at the wall and was more affected by vortices in the flow; therefore, for larger riblet spacings, it was easier for the fluid to travel in the cross-flow direction.

In figure 11(*c*) with the models with varying h^+, the taller riblets heights created lower cross-flow turbulence fluctuations. As the riblets became taller, the velocity at the riblet centre was less affected by the fluid above the riblets. The flow in tall riblets was less perturbed and resulted in more streamwise flow. In figure 11(*d*) with the models with varying t^+, modifying the riblet thickness minimally affected the turbulence fluctuations. Because the valley spacing was nearly the same in these cases, there was little difference in the turbulence fluctuations.

The reduction in turbulence fluctuations and the drag change trends did not match. According to the second possible mechanism, these plots were expected to match with a maximum drag reduction corresponding to a maximum reduction in turbulence fluctuations. For example, in the models with varying s^+, there was not an inflection in the reduction in turbulence fluctuations. In the models with varying riblet height, there was the same reduction in turbulence fluctuations for the baseline case and taller riblet case; however, one of these cases was a drag reduction while the other was a drag

https://doi.org/10.1017/jfm.2014.447 Published online by Cambridge University Press

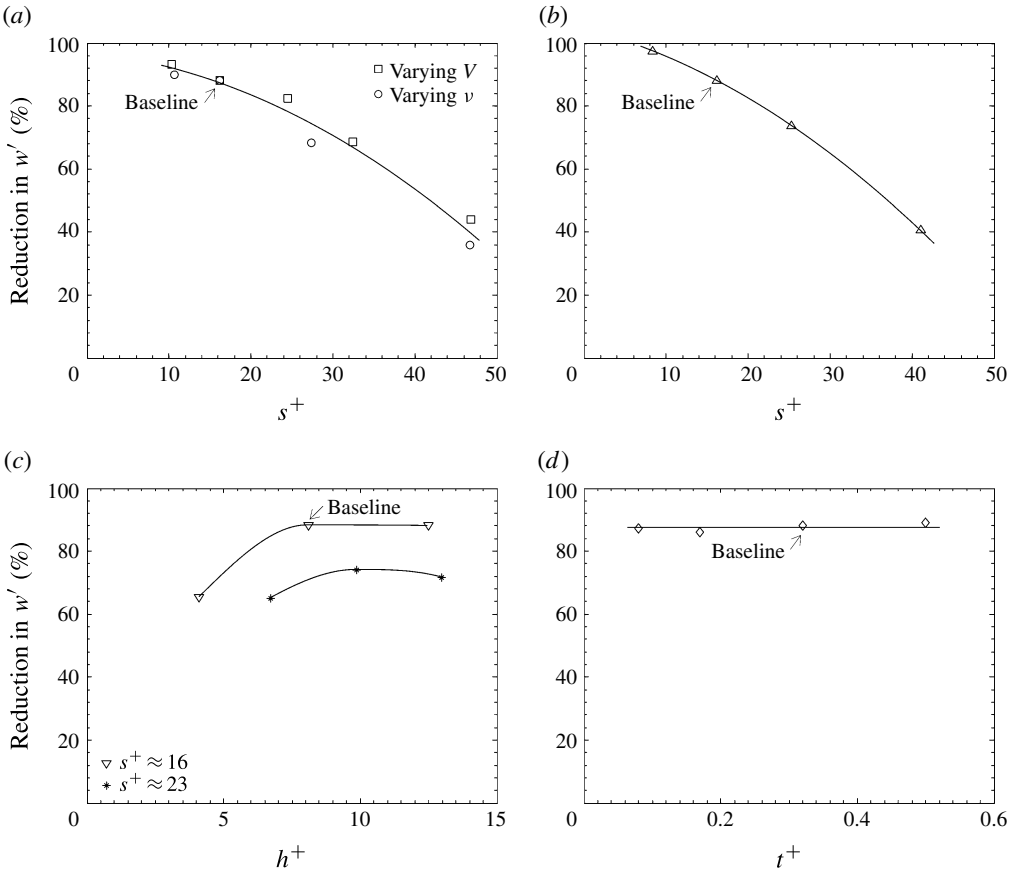


FIGURE 11. Cross-flow turbulence fluctuations for the various models. The data used in the analyses is for: (*a*) varying V or ν $s = 1.00$ mm, $h = 0.50$ mm, $t = 20.0$ μm, $Re = 2500$–$13\,000$; (*b*) varying s $h = 0.50$ mm, $t = 20.0$ μm, $\nu/V_l = 2.38$ μm, $Re = 4180$; (*c*) varying h downward-pointing triangle $s = 1.00$ mm, $t = 20.0$ μm, $\nu/V_l = 2.38$ μm, $Re = 4180$; asterisk $s = 0.75$ mm, $t = 15.0$ μm, $\nu/V_l = 1.20$ μm, $Re = 8360$; (*d*) varying t $s = 1.00$ mm, $h = 0.50$ mm, $\nu/V_l = 2.38$ μm, $Re = 4180$. A maximum in the turbulence fluctuations reduction should appear at the optimal drag reduction; however, the figures do not match this trend. Because this data does not match the drag change data, this method is not believed to be the drag reduction mechanism.

increase. Because the drag change and reduction in cross-flow turbulence fluctuations did not match, this idea was not thought to be the drag reduction mechanism in riblets.

The vortices and cross-flow turbulence fluctuations mechanisms may not be completely independent; however, from the simulations, the correlation between the two mechanisms was poor. Vortices generate ejecting and bursting motions which mixes high-velocity fluid with low-velocity fluid which increases drag. The presence of vortices near the wall could increase the cross-flow turbulence fluctuations. Vortices closer to the wall would have a larger effect on increasing cross-flow turbulence fluctuations than vortices further from the wall. It is thought that lifting vortices from the riblet surface is the primary mechanism rather than the channelling of flow in the streamwise direction as in the second mechanism.

https://doi.org/10.1017/jfm.2014.447 Published online by Cambridge University Press

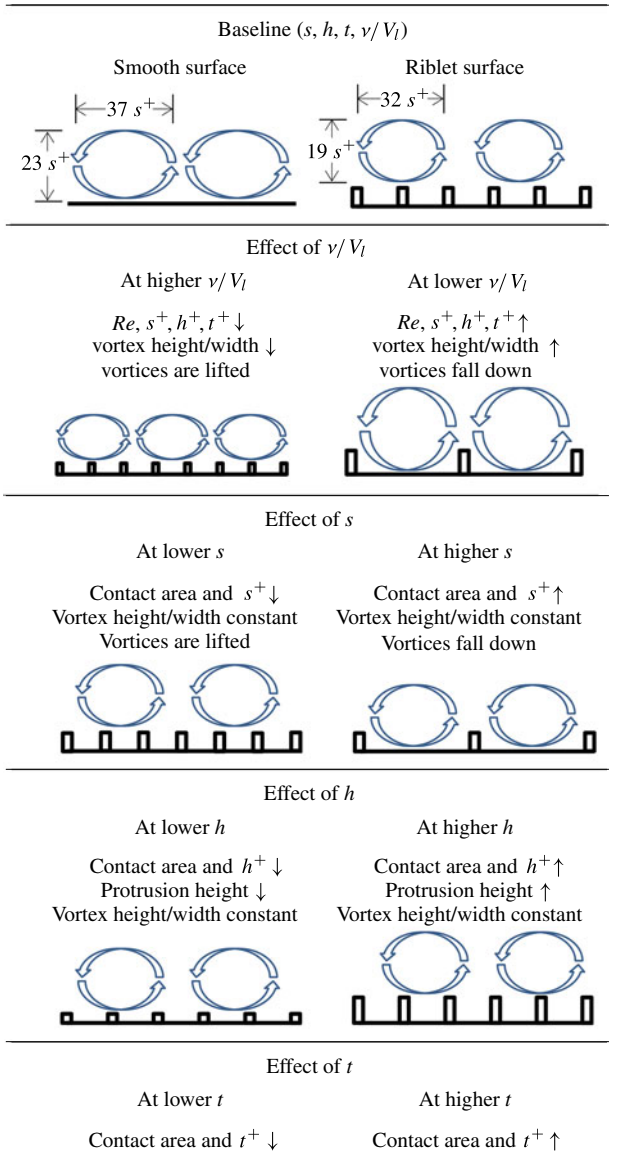


FIGURE 12. (Colour online) Conceptual models of various parameters effects on vortices (flow into the page, relative scale with average vortex size data). Drag reduction was obtained when vortices are lifted from the surface. Optimal riblet spacing was found to be when the vortex width was 1.5 times greater than the spacing with a riblet height $h^+ \approx 8$–10 which is near the lower boundary of the buffer layer. Minimal changes in drag and vortex height or width were found for tested values of t^+. At large values of t^+, the riblet spacing would be affected and increase drag.

3.4. *Effect of riblet geometry on vortices and flow properties*

Figure 12 shows a conceptual model of the effect of modifying the flow properties and riblet geometry on vortices. In the baseline case with Reynolds number based on channel height equal to 4180, the vortex height and width for the riblet and

https://doi.org/10.1017/jfm.2014.447 Published online by Cambridge University Press

smooth surfaces is given, as shown in figure 9. The sizes of the vortices for the other parameters are relative to this baseline case. By changing the velocity or viscosity term, the Reynolds number was affected which changes the vortex size. At high ν/V_l and therefore low Reynolds number, a small spacing and vortex size occurred; however, the spacing size decreased faster than the vortex size and so the vortices were lifted and a drag reduction case was exhibited. In the opposite case with low ν/V_l and therefore high Reynolds number, the spacing increased faster than the vortex size and so the vortices fell down and a drag increase case was exhibited, as shown in figure 9(*a*).

In the models with changing spacing, a smaller spacing was better than having a large spacing. Even though a small spacing had more surface area, it was more important to lift away the vortices from the surface. When the vortices were lifted from the surface, only the small contact area from the riblet peaks was exposed to high shear stress. In the models with varying spacing or height, the vortex size did not change because the Reynolds number based on channel height was constant, as shown in figure 9(*b,c*). Even though the riblet spacing and vortex size were the same between these cases, the models with varying height exhibited drastically different drag changes, as shown in figure 8(*c*). At low heights, the riblets lifted away the vortices from the surface and made it slightly more difficult for the high- and low-velocity fluids to mix. The riblets also do not protrude very far into the higher-velocity flow. In contrast, the taller riblets protrude into the higher-velocity flow and increase the surface area exposed to high drag.

The maximum drag reduction for each parameter's curve was approximately 10 %, and this drag reduction was similar to other optimal riblet drag reduction studies. According to Pollard (1998), this threshold in riblet drag reduction is due to the passive drag reduction nature of riblets. Even though riblets lift the vortices from the wall, there will still be some exchange of high- and low-velocity fluid in the valleys. The riblet mechanism lifts the majority of the turbulence from the wall, but does not significantly affect the turbulence production mechanism.

3.5. *Summary of riblet mechanism*

Figure 13 shows a summary figure with vortex sizes and drag change for varying riblet spacing. The data supports the first mechanism involving lifting of vortices by the riblet peaks, appropriately sized riblets lift the vortices from the surface decreasing the mixing of high-velocity and low-velocity fluid which leads to a drag reduction. The model with $s^+ = 25.3$ had a drag reduction of 11.7 %, whereas the model with $s^+ = 41.2$ had a drag reduction of 4.2 %. In both cases, the vortices are approximately the same size on the smooth and riblet surfaces. The parabolic curve fit for the drag change has a weaker drag reduction for small and large riblet spacings. At a small riblet spacing, the combination of greater surface area and vortices contacting many riblet peaks leads to a weaker drag reduction. At a large riblet spacing, the vortices fall within the riblet valley increasing drag which again leads to a weaker drag reduction. Eventually with even larger riblet spacings, a drag increase will be expected. A vortex width that was approximately 1.5 times the riblet spacing yielded an optimal drag reduction.

Based on the present study, optimal riblet spacing was in the range of $s^+ \approx 18$–25 and will depend on other riblet parameters. These values were on the same order to the maximum drag reduction spacing of $s^+ = 16$ (Bechert *et al.* 1997*b*)

https://doi.org/10.1017/jfm.2014.447 Published online by Cambridge University Press

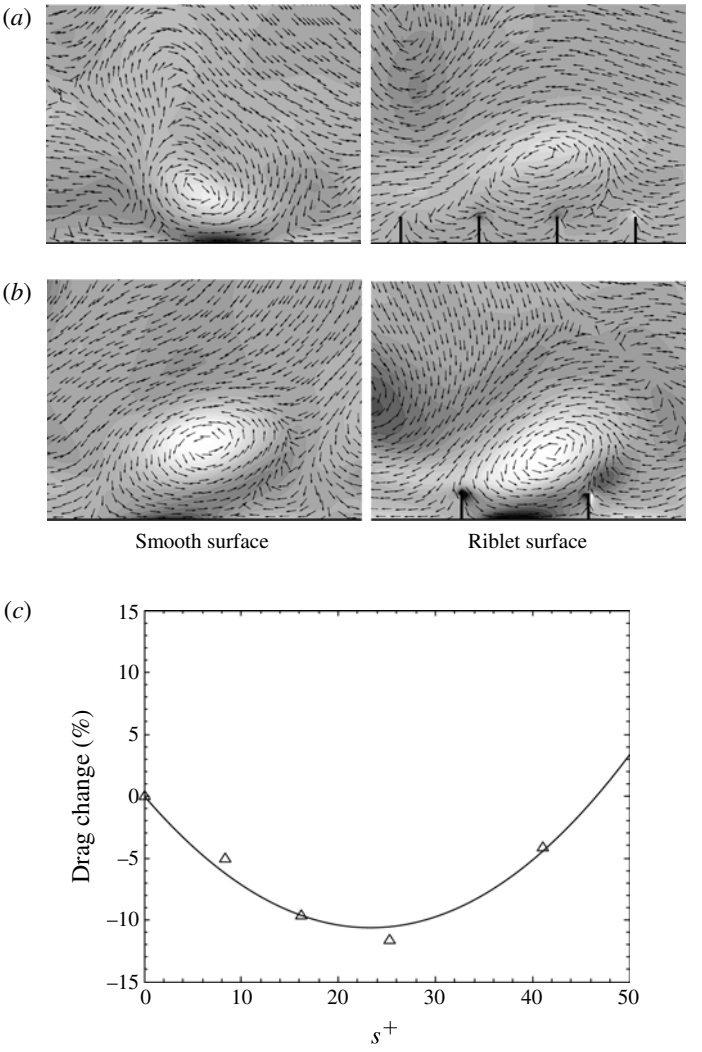


FIGURE 13. Vortices on the smooth and riblet surface with varying spacing along with the corresponding drag change for $h = 0.50$ mm, $t = 20.0$ μm, $\nu/V_l = 2.38$ μm and $Re = 4180$. Streamwise vorticity and tangential velocity vectors plotted to show vortices on smooth and riblet surfaces for (*a*) $s^+ = 25.3$ and (*b*) $s^+ = 41.2$. (*c*) Drag change for varying riblet spacing. Vortices are lifted from the surface with a smaller riblet spacing, but with a larger riblet spacing, the vortices fit within the riblet valley leading to greater drag and a weaker drag reduction. Increasing the riblet spacing even more will eventually lead to a drag increase.

and $s^+ = 17.7$ (El-Samni, Chun & Yoon 2007) for blade riblets. The riblet height should be calculated to stay in the range of $h^+ = 8$–10. In this range, the drag reduction was maximized; however, increasing the height and extending further into the channel quickly led to a drag increasing case. Because riblet thickness did not play a significant role at the tested thicknesses, the width of the riblet should be chosen to be durable enough for the application.

https://doi.org/10.1017/jfm.2014.447 Published online by Cambridge University Press

4. Conclusions

The scales of fast-swimming sharks have been shown to provide a drag-reduction benefit over a smooth plate (Bechert *et al.* 2000*b*; Jung & Bhushan 2009). These scales have riblet structures with microgrooves that efficiently control the flow of water and have shown drag reductions of up to 10 %. In prior studies, two prevalent drag-reduction mechanisms have been presented. In the first mechanism, appropriately sized riblets lift vortices from the surface decreasing eject and sweep motions associated with high shear stress and drag. In the second mechanism, riblets channel the flow and reduce the cross-flow turbulence fluctuations. To study these mechanisms and the effect of riblet geometry and flow properties on drag, vortices and turbulence fluctuations, computational models were created.

In this research, the data agreed with the first mechanism and disagreed with the second mechanism. When the vortices were approximately 1.5 times as large as the riblet spacing, optimal drag reduction was observed. The largest drag reductions occurred when the riblet spacing was $s^+ \approx 18$–25 and $h^+ \approx 8$–10 which was on the same order to $s^+ = 16$ and $h^+ = 8$ from Bechert *et al.* (1997*b*) and $s^+ = 18$ and $h^+ = 9$ from El-Samni *et al.* (2007). As the vortices approached and became smaller than the spacing size, the riblet surface became a drag increasing case. In the second mechanism, the cross-flow turbulence fluctuations were measured and compared with the drag change. Because the cross-flow turbulence fluctuations and drag change trends did not match, it showed that this mechanism did not adequately explain the riblet drag-reduction mechanism.

The average vortex size is believed to be dependent on Reynolds number based on channel height with smaller vortices on the riblet surface than the smooth surface due to riblets obstructing vortex rotation and growth. For both surfaces as Reynolds number increased, vortex size increased. In addition to choosing appropriate riblet spacing, the height needed to be $h^+ = 8$–10 for optimal drag reduction. Increasing the height quickly led to a drag increasing case due to the riblets protruding further into the higher-velocity flow. The thickness parameter had little effect on the drag change at the tested values due to the much larger surface area in the riblet valleys.

By independently changing the velocity, viscosity, spacing, height and thickness parameters, it was observed that the non-dimensional definition was valid. Comparable drag changes were observed for similar non-dimensional spacings that were created by modifying the velocity, viscosity or spacing variables; therefore, the non-dimensional parameters can be used to determine drag change in an application.

A better understanding of the riblet mechanism of controlling the streamwise vortices and the effect of riblet geometry and flow properties on riblet drag reduction will expand riblet usage. Optimal drag reduction is believed to occur when the vortex width is 1.5 times the riblet spacing and riblet height of $h^+ = 8$–10. With streamwise vortex diameters of approximately 30 non-dimensional units, this leads to $s^+ = 20$ and keeping the riblet height $h^+ = 8$–10. These riblet design principles can be applied in various commercial applications such as marine, medical and industrial fields as a method to reduce drag.

Acknowledgements

The authors would like to thank the Ohio State University for their university fellowship support to the first author, Dr G. Bixler and Professor S. Mazumder for their insightful discussion, and B. Woodall for Ohio Supercomputer Center (OSC) support. This work was supported in part by an allocation of computing time from the OSC.

https://doi.org/10.1017/jfm.2014.447 Published online by Cambridge University Press

Nomenclature

s	Dimensional riblet spacing (peak-to-peak distance)
h	Dimensional riblet height (peak-to-valley distance)
t	Dimensional riblet thickness (peak width)
s^+	Non-dimensional riblet spacing (peak-to-peak distance)
h^+	Non-dimensional riblet height (peak-to-valley distance)
t^+	Non-dimensional riblet thickness (peak width)
v_τ	Wall shear-stress velocity
ν	Kinematic viscosity
$\Delta\tau$	Difference in shear stress between the riblet and smooth surfaces
τ_0	Shear stress for the smooth surface
ρ	Fluid density
V	Average velocity in the streamwise direction
V_l	Centreline velocity of a laminar parabolic profile
Q	Instantaneous volume flux
A_c	Cross-sectional area of the riblet model
H	Height of the riblet model
W	Width of the riblet model
L	Length of the riblet model
δ	Channel half-width of the riblet model
Re	Reynolds number based on channel height
ΔT	Dimensional time step
T^+	Non-dimensional time
Δh	Effective protrusion height parameter
h_{ps}	Streamwise protrusion height
h_{pc}	Cross-flow protrusion height
D	Edge length of the square cylinder
$\bar{C}_L$	Mean lift coefficient
C_L^{rms}	Lift oscillation amplitude
$\bar{C}_D$	Mean drag coefficient
C_D^{rms}	Drag oscillation amplitude
St	Strouhal number
D_s	Instantaneous skin-friction drag for the smooth surface
D_r	Instantaneous skin-friction drag for the riblet surface
w_s'	Root-mean-square cross-flow turbulence fluctuation on the smooth surface
w_r'	Root-mean-square cross-flow turbulence fluctuation on the riblet surface

REFERENCES

AUTUMN, K., DITTMORE, A., SANTOS, D., SPENKO, M. & CUTKOSKY, M. 2006 Frictional adhesion: a new angle on gecko attachment. *J. Expl Biol.* **209**, 3569–3579.

AUTUMN, K., LIANG, Y. A., HSIEH, S. T., ZESCH, W., CHAN, W. P., KENNY, T. W., FEARING, R. & FULL, R. J. 2000 Adhesive force of a single gecko foot-hair. *Nature* **405**, 681–685.

https://doi.org/10.1017/jfm.2014.447 Published online by Cambridge University Press

BECHERT, D. & BARTENWERFER, M. 1989 The viscous flow on surfaces with longitudinal ribs. *J. Fluid Mech.* **206**, 105–129.

BECHERT, D., BARTENWERFER, M., HOPPE, G. & REIF, W. E. 1986 Drag reduction mechanisms derived from shark skin. In *ICAS, Congress, 15th, London, England, September 7–12, 1986, Proceedings. Vol. 2 (A86-48976 24-01)*, pp. 1044–1068. American Institute of Aeronautics and Astronautics, Inc.

BECHERT, D., BRUSE, M., HAGE, W. & MEYER, R. 1997*a* Biological Surfaces and Their Technological Application Laboratory and Flight Experiments on Drag Reduction and Separation Control, *Paper #AIAA-1997-1960, presented at AIAA 28th Fluid Dynamics Conference*, Snowmass Village, CO, AIAA, New York.

BECHERT, D., BRUSE, M. & HAGE, W. 1997*b* Experiments on drag-reducing surfaces and their optimization with an adjustable geometry. *J. Fluid Mech.* **338**, 59–87.

BECHERT, D., BRUSE, M. & HAGE, W. 2000*a* Experiments with three-dimensional riblets as an idealized model of shark skin. *Exp. Fluids* **28**, 403–412.

BECHERT, D., BRUSE, M. & HAGE, W. 2000*b* Fluid mechanics of biological surfaces and their technological application. *Naturwissenschaften* **87**, 157–171.

BECHERT, D., HOPPE, G., VAN DER HOEVEN, J. T. & MAKRIS, R. 1992 The Berlin oil channel for drag reduction research. *Exp. Fluids* **12**, 251–260.

BHUSHAN, B. 2009 Biomimetics: lessons from nature – an overview. *Phil. Trans. R. Soc. Lond.* A **367**, 1445–1486.

BHUSHAN, B. 2010 *Springer Handbook of Nanotechnology*, 3rd edn. Springer.

BHUSHAN, B. 2012 *Biomimetics: Bioinspired Hierarchical-Structured Surfaces for Green Science and Technology*. Springer.

BIXLER, G. D. & BHUSHAN, B. 2012*a* Biofouling: lessons from nature. *Phil. Trans. R. Soc. Lond.* A **370**, 2381–2417.

BIXLER, G. D. & BHUSHAN, B. 2012*b* Bioinspired rice leaf and butterfly wing surface structures combining shark skin and lotus effects. *Soft Matt.* **8**, 11271–11284.

BIXLER, G. D. & BHUSHAN, B. 2013 Shark skin inspired low-drag microstructured surfaces in closed channel flow. *J. Colloid Interface Sci.* **393**, 384–396.

CHENG, C., LU, P. & CHEN, R. 1992 Wind loads on square cylinder in homogeneous turbulent flows. *J. Wind Engng Ind. Aerodyn.* **41**, 739–749.

CHOI, H., MOIN, P. & KIM, J. 1993 Direct numerical simulation of turbulent flow over riblets. *J. Fluid Mech.* **255**, 503–539.

CHU, D. C. & KARNIADAKIS, G. E. 1993 A direct numerical simulation of laminar and turbulent flow over riblet-mounted surfaces. *J. Fluid Mech.* **250**, 1–42.

DEAN, B. & BHUSHAN, B. 2010 Shark-skin surfaces for fluid-drag reduction in turbulent flow: a review. *Phil. Trans. R. Soc. Lond.* A **368**, 4775–4806.

EL-SAMNI, O. A., CHUN, H. H. & YOON, H. S. 2007 Drag reduction of turbulent flow over thin rectangular riblets. *Intl J. Engng Sci.* **45**, 436–454.

FLUENT 2014 ANSYS® FLUENT, Release 14.0, Help System, FLUENT User's Guide, ANSYS, Inc.

GAO, H., WANG, X., YAO, H., GORB, S. & ARZT, E. 2005 Mechanics of hierarchical adhesion structures of geckos. *Mech. Mater.* **37**, 275–285.

GARCÍA-MAYORAL, R. & JIMÉNEZ, J. 2011 Drag reduction by riblets. *Phil. Trans. R. Soc. Lond.* A **369**, 1412–1427.

GENZER, J. & EFIMENKO, K. 2006 Recent developments in superhydrophobic surfaces and their relevance to marine fouling: a review. *Biofouling* **22**, 339–360.

GOLDSTEIN, D., HANDLER, R. & SIROVICH, L. 1995 Direct numerical simulation of turbulent flow over a modelled riblet-covered surface. *J. Fluid Mech.* **302**, 333–376.

JIMENEZ, J. & MOIN, P. 1991 The minimal flow unit in near-wall turbulence. *J. Fluid Mech.* **225**, 213–240.

JUNG, Y. C. & BHUSHAN, B. 2009 Biomimetic structures for fluid drag reduction in laminar and turbulent flows. *J. Phys.: Condens. Matter* **22**, 035104.

https://doi.org/10.1017/jfm.2014.447 Published online by Cambridge University Press

KIM, J., MOIN, P. & MOSER, R. 1987 Turbulence statistics in fully developed channel flow at low Reynolds number. *J. Fluid Mech.* **177**, 133–166.

KRIEGER, K. 2004 Do pool sharks swim faster? *Science* **305**, 636–637.

LEE, B. 1975 The effect of turbulence on the surface pressure field of a square prism. *J. Fluid Mech.* **69**, 263–282.

LEE, S.-J. & LEE, S.-H. 2001 Flow field analysis of a turbulent boundary layer over a riblet surface. *Exp. Fluids* **30**, 153–166.

LYN, D. A., EINAV, S., RODI, W. & PARK, J. 1995 A laser-Doppler velocimetry study of ensemble-averaged characteristics of the turbulent near wake of a square cylinder. *J. Fluid Mech.* **304**, 285–319.

LYN, D. & RODI, W. 1994 The flapping shear layer formed by flow separation from the forward corner of a square cylinder. *J. Fluid Mech.* **267**, 353–376.

MCLEAN, I. & GARTSHORE, I. 1992 Spanwise correlations of pressure on a rigid square section cylinder. *J. Wind Engng Ind. Aerodyn.* **41**, 797–808.

MURAKAMI, S. & MOCHIDA, A. 1995 On turbulent vortex shedding flow past 2D square cylinder predicted by CFD. *J. Wind Engng Ind. Aerodyn.* **54**, 191–211.

OCHOA, J. & FUEYO, N. 2004 Large-Eddy Simulation of the flow past a square cylinder. In *PHOENICS 10th International User Conference Melbourne, Australia, CHAM Limited, London*.

POLLARD, A. 1998 Passive and active control of near-wall turbulence. *Prog. Aerosp. Sci.* **33**, 689–708.

REIF, W. E. 1985 *Squamation and Ecology of Sharks*. E. Schweizerbartsche Verlagsbuchhandlung.

ROBINSON, S. K. 1990 A review of vortex structures and associated coherent motions in turbulent boundary layers. In *Structure of Turbulence and Drag Reduction*, pp. 23–50. Springer.

ROBINSON, S., KLINE, S. J. & SPALART, P. 1989 A review of quasi-coherent structures in a numerically simulated turbulent boundary layer. *NASA STI/Recon Tech. Rep.* N 90: 13723.

RODI, W. 1997 Comparison of LES and RANS calculations of the flow around bluff bodies. *J. Wind Engng Ind. Aerodyn.* **69**, 55–75.

RODI, W., FERZIGER, J., BREUER, M. & POURQUIE, M. 1997 Status of large eddy simulation: results of a workshop. *Trans. ASME J. Fluids Engng* **119**, 248–262.

ROHR, J., ANDERSEN, G., REIDY, L. & HENDRICKS, E. 1992 A comparison of the drag-reducing benefits of riblets in internal and external flows. *Exp. Fluids* **13**, 361–368.

SPALDING, D. B. 1961 A single formula for the law of the wall. *Trans. ASME J. Appl. Mech.* **28**, 455–458.

SUZUKI, Y. & KASAGI, N. 1994 Turbulent drag reduction mechanism above a riblet surface. *AIAA J.* **32**, 1781–1790.

VICKERY, B. 1966 Fluctuating lift and drag on a long cylinder of square cross-section in a smooth and in a turbulent stream. *J. Fluid Mech.* **25**, 481–494.

WALSH, M. J. 1982 Turbulent Boundary Layer Drag Reduction using Riblets, Paper #AIAA-1982-0169, presented at AIAA 20th Aerospace Sciences Meeting, Orlando FL, AIAA, New York.

WALSH, M. J. & ANDERS, J. B. JR 1989 Riblet/LEBU research at NASA Langley. *Appl. Sci. Res.* **46**, 255–262.

WEISS, M. H. 1993 Drag reduction with riblets in pipe flow. PhD Diss., University of Calgary, Alberta, Canada.

WEISS, M. 1997 Implementation of drag reduction techniques in natural gas pipelines. In *10th European Drag Reduction Working Meeting, Berlin, Germany, 19–21 March*.

https://doi.org/10.1017/jfm.2014.447 Published online by Cambridge University Press